Catal Lett
DOI 10.1007/s10562-016-1695-8

Effect of an Alumina Phase on the Reductive Amination of 2-Propanol to Monoisopropylamine Over Ni/Al_2O_3

Jun Hee Cho[1] · Sang Hee An[1] · Tae-Sun Chang[2] · Chae-Ho Shin[1]

Received: 4 September 2015 / Accepted: 18 January 2016

Abstract Various single-phase aluminum oxides were prepared through the thermal decomposition of bayerite, boehmite, and gibbsite. $Ni/\gamma\text{-}Al_2O_3$ and $Ni/\delta\text{-}Al_2O_3$ catalysts exhibited higher monoisopropylamine (MIPA) selectivity than the η-, θ-, and $\kappa\text{-}Al_2O_3$ supported Ni catalysts for the reductive amination of 2-propanol (IPA) in the presence of hydrogen and ammonia. FT-IR spectra after pyridine adsorption showed that a high number of Lewis acid sites could be correlated with enhancement in MIPA selectivity. $Ni/\eta\text{-}Al_2O_3$ and $Ni/\gamma\text{-}Al_2O_3$ catalysts exhibited the highest catalytic activity arising from differences in the metallic surface area. Both catalyst activity and selectivity with regards to reductive amination were strongly affected by the nature of the support.

Graphical Abstract

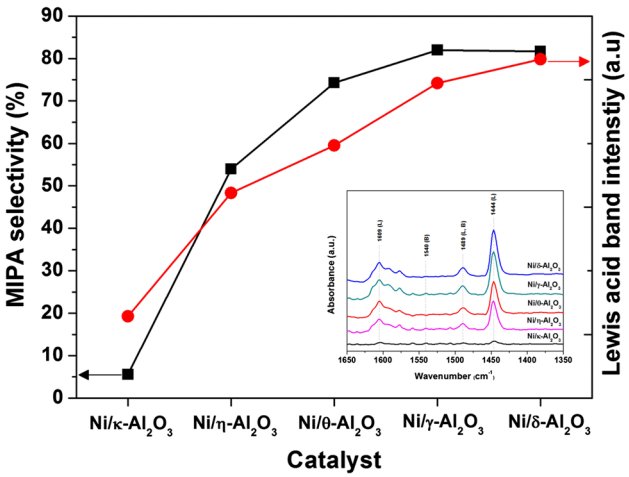

Keywords 2-Propanol · Alumina phase · Reductive amination · Nickel · Monoisopropylamine

1 Introduction

Alkyl amines are used widely as intermediates for the synthesis of herbicides, insecticides, and drugs. Their other applications include rubber accelerators, corrosion inhibitors, and surface-active agents. They can be obtained by the reductive amination of aliphatic alcohols or carbonyl compounds using ammonia in the presence of hydrogen. However, yields and selectivities are rather low in the synthesis of amines from their corresponding alcohols. The production of primary amines from alcohols and ammonia would be a very desirable process if it could be performed

Electronic supplementary material The online version of this article (doi:10.1007/s10562-016-1695-8) contains supplementary material, which is available to authorized users.

✉ Chae-Ho Shin
chshin@chungbuk.ac.kr

Jun Hee Cho
dnvk@nate.com

Sang Hee An
anll59@nate.com

Tae-Sun Chang
tschang@krict.re.kr

[1] Department of Chemical Engineering, Chungbuk National University, Cheongju, Chungbuk 28644, Korea

[2] Environment & Resources Research Center, Korea Research, Institute of Chemical Technology, Daejon 34102, Korea

Published online: 16 February 2016

with high selectivity for the amines [1–5]. Ni/Al_2O_3 catalysts have been used widely in CH_4 reforming, glycerol steam reforming, and CO methanation [6–9].

Synthesis of monoisopropylamine (MIPA) via reductive amination of *iso*-propanol (IPA) with ammonia is performed over a supported metal catalyst, typically nickel or cobalt on silica and alumina, at temperatures of 190–250 °C and pressures of 18–50 bar [9]. The conversion of IPA into MIPA includes three major reaction steps: (1) dehydrogenation to form acetone, (2) condensation with ammonia to form an imine, and (3) hydrogenation to form MIPA. Each intermediate and MIPA can undergo various side reactions such as condensation, decarbonylation, disproportionation, and hydrogenolysis [10].

The reductive amination of alcohols over nickel-based catalysts has been studied using supports such as alumina, silica, silica-alumina, zirconia, and zeolite [11–13]. Among the various supports, Al_2O_3 has reasonably good mechanical properties due to its thermal stability [14, 15]. The choice of alumina as the catalyst support material also affects activity and selectivity in the reductive amination [6]. According to earlier studies, these support effects may be due to changes in metal particle sizes and morphologies, or interactions between the carrier and the supported metal. In addition, amine selectivity is influenced by the acid–base properties of the support [16–20]. Shimizu et al. [19] investigated the direct synthesis of primary amines from 2-octanol with ammonia over Ni based catalyst showing that the support properties such as acid–base sites influenced to selectivity of primary amine.

In our previous work, we examined the effects of nickel loading in the reductive amination of IPA over $Ni/\gamma\text{-}Al_2O_3$ catalysts and proposed that 17 wt% $Ni/\gamma\text{-}Al_2O_3$ catalysts were the most active [21]. No comparison work has been conducted for the reductive amination of IPA over Ni catalysts supported on alumina with different crystalline phases. The objective was to study the interaction of nickel particles with different alumina phases and to explore any relationships between catalyst performance and support properties.

2 Experimental

2.1 Support Preparation

Various single-phase aluminum oxides were prepared through thermal decomposition of bayerite, boehmite, and gibbsite. Bayerite was prepared by the precipitation method at room temperature. NH_4OH (Samchun, ≥28 %) was added slowly until 1.0 M $Al(NO_3)_2{\cdot}6H_2O$ (Junsei) solution reached pH 10, which was then maintained for 10 days with vigorous stirring. The resultant white precipitate was filtered and washed with deionized water. The obtained precipitate was dried in an oven at 100 °C for 24 h. Boehmite (Sasol) and gibbsite (Samchun Chem.) were used as purchased. We prepared $\eta\text{-}Al_2O_3$ through the calcination of bayerite at 600 °C for 4 h. $\kappa\text{-}Al_2O_3$ was obtained after gibbsite was calcined at 1000 °C for 4 h. We prepared $\delta\text{-}Al_2O_3$ through the calcination of boehmite at 950 °C. $\theta\text{-}Al_2O_3$ was obtained after calcination of $\gamma\text{-}Al_2O_3$ (Sasol) at 1050 °C for 2 h.

2.2 Catalyst Preparation

Commercial $\gamma\text{-}Al_2O_3$ (Procatalyse) was used as a support. $\eta\text{-}Al_2O_3$, $\kappa\text{-}Al_2O_3$ [18], $\delta\text{-}Al_2O_3$, and $\theta\text{-}Al_2O_3$ were prepared as described above and utilized as supports. Ni/Al_2O_3 catalysts were prepared by incipient wetness impregnation using $Ni(NO)_3{\cdot}6H_2O$ (Sigma-Aldrich) solution. The concentration of the impregnation solution was adjusted to obtain a nickel loading of 17 wt%. The impregnated catalysts were dried at 100 °C overnight and subsequently calcined at 500 °C for 2 h in a muffle furnace under flowing air.

2.3 Catalyst Characterization

Supports and catalysts were degassed for 6 h at 250 °C before measurement and their Brunauer–Emmett–Teller (BET) surface areas, pore volumes, and pore size distributions were determined by N_2 physisorption at −196 °C using Micromeritics ASAP2020 apparatus. Surface areas were calculated in the range of $P/P_o = 0.03–0.2$. Pore size distributions were calculated from the desorption branch using Barrett–Joyner–Halenda (BJH) formulism. X-ray diffraction patterns were obtained on a Rigaku diffractometer using Cu Kα radiation operating at 40 kV and 40 mA, with a scanning rate of 5 degree min^{-1} from 20° to 80°, to identify the crystalline phases of supports and catalysts. Calcined catalysts, as well as those reduced at 600 °C for 3 h under H_2 flow (50 cm^3 min^{-1}) followed by passivation with 1.0 % O_2/He for 0.5 h at room temperature (RT), were characterized separately to identify the crystalline phases of NiO and Ni metal. H_2-temperature-programmed reduction (H_2-TPR) using a Micromeritics AutoChem II 2920 instrument determined the reducibility of nickel oxides. Before measurement, each sample (0.1 g) was pretreated under flowing He (50 cm^3 min^{-1}) up to 400 °C and held at that temperature for 1 h, to remove adsorbed water and other contaminants, before being cooled to 30 °C under flowing He. Reducing gas containing 5 % H_2/Ar mixture (50 cm^3 min^{-1}) was then passed over while heating to 800 °C at a rate of 10 °C min^{-1}. A thermal conductivity detector (TCD) determined the amount of H_2 consumed.

The dispersion of nickel and the nickel surface area were measured by H_2 chemisorption at 100 °C under static conditions using a Micromeritics ASAP 2020C instrument equipped with a high-vacuum pump, providing a vacuum of 10^{-6} Torr. Prior to adsorption experiments, each 0.3 g sample was reduced at 600 °C for 3 h. H_2 chemisorption uptakes were separately determined as the difference of two successive isotherm measurements. Metal dispersion and the nickel metal surface area were calculated assuming a H/Ni stoichiometry of 1. The degree of reduction was determined by O_2 titration using the following equation: [amount of O_2 consumed]/[theoretical amount of H_2 consumed assuming nickel oxides fully reduced (mmol H_2; $NiO + H_2 \rightarrow Ni + 2H^+$)] × 100), and used to correct the nickel particles sizes [22, 23].

The surface acidity of the Ni/Al_2O_3 catalysts reduced at 600 °C was measured with a Biorad 175C FT-IR spectrometer after pyridine adsorption. A self-supported sample was prepared by pressing, and then treated under flowing He (100 cm^3 min^{-1}) and H_2 (20 cm^3 min^{-1}) at 400 °C for 1 h in situ in an IR cell. After cooling to 50 °C, the pretreated samples were exposed to pyridine vapor, and then evacuated for 0.5 h at 50 °C. After treatment, IR spectra were obtained at ambient temperature.

The morphology of Ni/Al_2O_3 catalysts was examined with an Ultra High Resolution FE-SEM (Carl Zeiss, Resolution : 0.8 nm at 15 kV) and the energy dispersive X-ray Analysis (EDS) mapping of Ni/Al_2O_3 catalysts was carried out with a JEOL JSM-7000F (Resolution; 133 eV).

2.4 Catalytic Activity Tests

All catalytic experiments were performed under atmospheric pressure at continuous-flow in a fixed bed microreactor. Prior to testing, the catalysts were activated at 600 °C for 3 h under a flow of purified H_2 (50 cm^3 min^{-1}) and kept at the desired temperature to establish a standard operating procedure, allowing time for product distribution to stabilize. Standard conditions involved the following reaction parameters: $T = 160$ °C; weight hourly space velocity (WHSV, h^{-1}) = 4.3; and feed composition ($IPA/NH_3/H_2/N_2$; molar ratio) = 1/4/6/22.8. The partial pressure of IPA was fixed at 3 kPa.

For the comparison of selectivities of MIPA over various Ni/Al_2O_3 catalysts, space velocity was controlled in the range 2.3–19.1 at 150 °C. To maintain constant partial pressures of the reactants, nitrogen was used as a diluent. The reaction products were analyzed on-line using a Chrompack-CP-9001 gas chromatograph equipped with a CP-Volamine capillary column (60 mm × 0.32 mm) and a flame ionization detector. The conversion of IPA, selectivity and WHSV were defined as follows:

$$Conversion(\%) = \frac{F_{\mathrm{IPA}} reacted}{F_{\mathrm{IPA}} fed} \times 100\%$$

$$iComponent\ selectivity(\%) = \frac{F_i C_i}{\Sigma F_i C_i} \times 100\ \%$$

$$\mathrm{WHSV}\ \left(h^{-1}\right) = \frac{F_{\mathrm{IPA}}\left(\mathrm{mol\ h^{-1}}\right) \times \mathrm{MW_{IPA}}\left(\mathrm{g\ mol^{-1}}\right)}{Quantity\ of\ catalyst(g)}$$

where F_{IPA} and F_i are molar flow rates of IPA and i products which are MIPA, diisopropylamine (DIPA), acetone, respectively. MW_{IPA} is a molecular weight of IPA. C_i is a carbon number of i products.

3 Results and Discussion

3.1 Physical Properties of Alumina

X-ray diffraction patterns for various Al_2O_3 supports are shown in Fig. 1. The alumina phases, i.e. θ-Al_2O_3, δ-Al_2O_3, γ-Al_2O_3, η-Al_2O_3 and κ-Al_2O_3, were identified

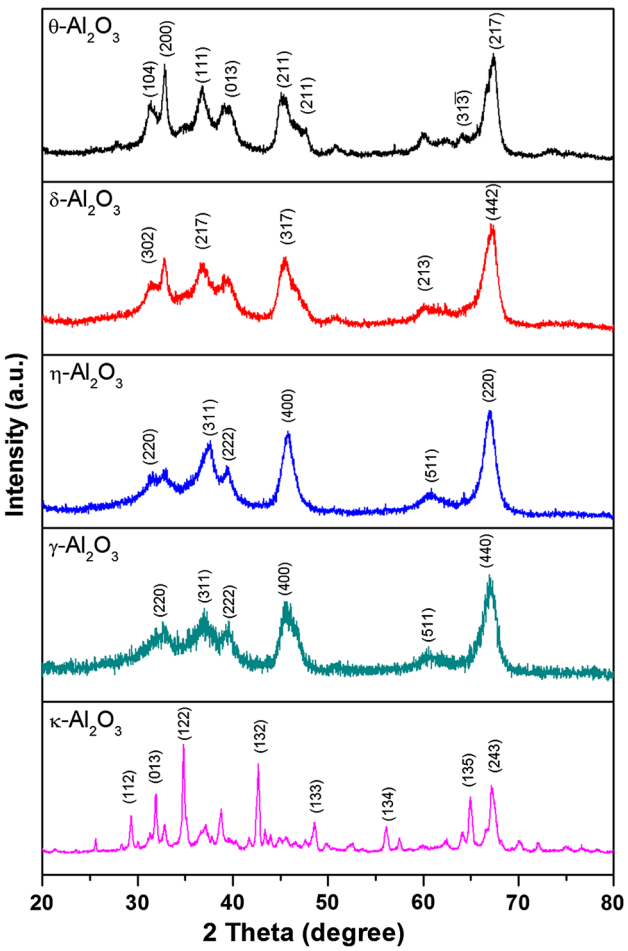

Fig. 1 X-ray diffraction patterns of alumina supports prepared by thermal decomposition of bayerite, boehmite, and gibbsite

based on the highest intensities. Each alumina support has its own characteristic bulk crystal structure [16, 24, 25]. It has been reported that γ-Al_2O_3 and η-Al_2O_3 have similar crystal structures and that η-Al_2O_3 has a sharper (111) peak than γ-Al_2O_3 [16], which is consistent with our results. The summarized results of the surface area and pore volume for Al_2O_3 supports are shown in Table 1, and the BJH pore size distribution is shown in Fig. 2. The surface area increased in the following order: κ-Al_2O_3 < θ-Al_2O_3 < δ-Al_2O_3 < η-Al_2O_3 < γ-Al_2O_3. All of the supports exhibited hysteresis during the adsorption and desorption processes (data not shown). The pore size distributions were narrow, with ranges limited to less than 30 nm, except for the κ-Al_2O_3 support, where the pore size distribution ranged from 20 to 100 nm. The η-Al_2O_3 and γ-Al_2O_3 supports exhibited bimodal pore types.

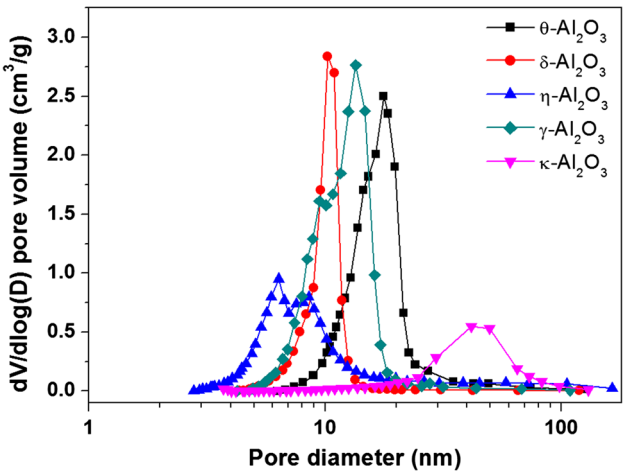

Fig. 2 Pore size distribution of various alumina supports used in this study: θ-Al_2O_3, δ-Al_2O_3, η-Al_2O_3, γ-Al_2O_3, and κ-Al_2O_3

3.2 Characterization of Ni/Al_2O_3 Catalysts

The physical properties of calcined Ni/Al_2O_3 are summarized in Table 1. BET surface area, pore volume, and pore size progressively decreased after impregnation and calcination. The Ni/Al_2O_3 catalysts showed reduced pore volume and average pore size, which means there was efficient deposition of nickel species in the inner pores of the Al_2O_3 support. Although pore volume and size after nickel impregnation decreased, the surface area of the Ni/κ-Al_2O_3 catalysts decreased slightly, from 23 to 22 $m^2\ g^{-1}$. This was probably due to the deposition of large nickel particles on the outer surface of the κ-Al_2O_3 [26].

The XRD patterns of the various Ni/Al_2O_3 catalysts calcined at 500 °C and reduced at 600 °C are shown in Fig. 3. The calcined catalysts exhibited a characteristic reflection peak at $2\theta = 43.2°$ due to the presence of the NiO (JCPDS 47-1049) phase. The present XRD analysis suggested that there was no new compound formed between nickel oxide and the alumina. The average particle size of NiO was estimated using the Scherrer equation. As shown in Table 2, the average particle size of NiO ranged from 9.5 to 18.0 nm. Larger NiO particle sizes of around 18.0 nm were observed in the Ni/κ-Al_2O_3 catalyst, and the minimum size observed in the Ni/η-Al_2O_3 catalyst was around 9.6 nm, with the exception of the Ni/γ-Al_2O_3 support. This observation is consistent with the pore size measurement from the BJH method. The smaller nickel oxide particles deposited on the η-Al_2O_3 support was attributed to the small pore sizes in the Ni/η-Al_2O_3 catalyst [18, 26]. The Ni/γ-Al_2O_3 catalyst, with a larger specific surface, had a smaller average particle size. The reduced Ni/Al_2O_3 catalysts showed the characteristics peaks for metallic Ni (JCPDS 04-0850) and Al_2O_3. Before and after the reduction, the alumina phase of all catalysts was nearly the same. This indicated that the crystal phase of the alumina supports had not changed during reduction at 600 °C for 3 h. The diffraction peaks of Ni metal gradually became sharper and more intense in the following order: Ni/η-Al_2O_3 < Ni/γ-Al_2O_3 < Ni/θ-Al_2O_3 < Ni/δ-Al_2O_3 < Ni/κ-Al_2O_3. Among the catalysts examined, the Ni/η-Al_2O_3 catalyst exhibited the smallest Ni particle size of 8.7 nm, whereas the Ni/κ-Al_2O_3 catalyst had the largest Ni particle size of 18.7 nm.

Table 1 Physical properties of alumina supports and Ni/Al_2O_3 catalysts

Catalysts	S_{BET} ($m^2\ g^{-1}$)	Pore volume ($cm^2\ g^{-1}$)	Pore diameter (nm)	Supports		
				S_{BET} ($m^2\ g^{-1}$)	Pore volume ($cm^2\ g^{-1}$)	Pore diameter (nm)
Ni/θ-Al_2O_3	83	0.353	17.1	109	0.519	19.0
Ni/δ-Al_2O_3	93	0.256	11.1	117	0.362	12.3
Ni/η-Al_2O_3	105	0.253	9.6	143	0.369	10.3
Ni/γ-Al_2O_3	144	0.472	13.1	194	0.699	14.4
Ni/κ-Al_2O_3	22	0.159	28.0	23	0.205	35.8

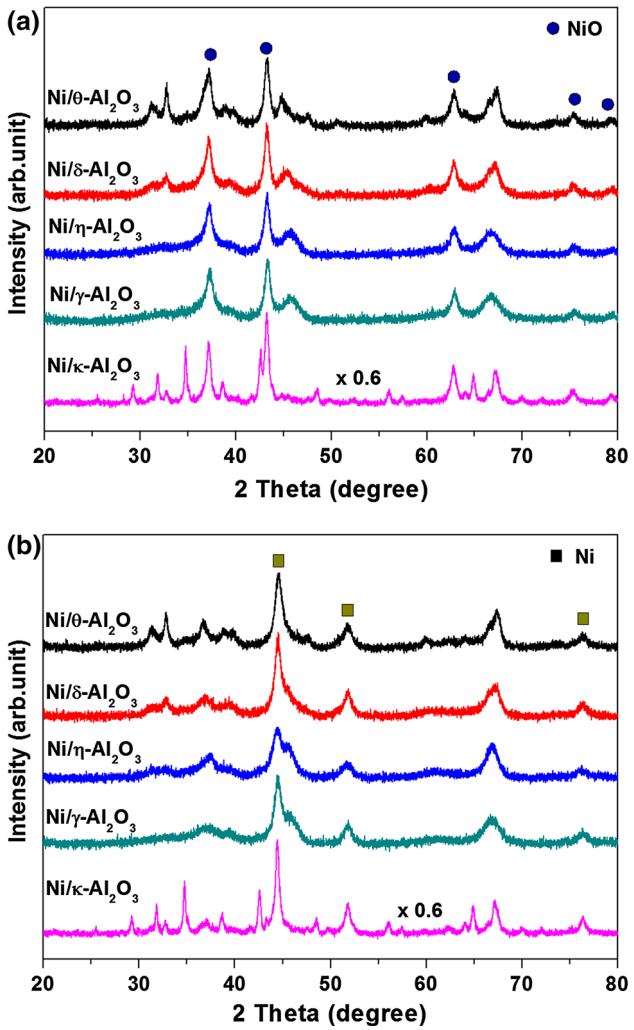

Fig. 3 XRD patterns of Ni/Al_2O_3 catalysts with various alumina supports **a** calcined at 500 °C for 2 h, and **b** reduced at 600 °C for 3 h

The H_2-TPR profiles of calcined Ni/Al_2O_3 catalysts with different alumina phase supports are shown in Fig. 4. The TPR data revealed that different alumina phase supports influence the reduction behavior of the catalysts. The reducibility of the catalysts was compared as part of the evaluation of interactions between nickel and the supports. The TPR profiles of the Ni/Al_2O_3 catalysts calcined at 500 °C revealed that three main reduction peaks were observed with a temperature range of 300–450, 450–650, and 650–750 °C with broad reduction profiles, except for the Ni/κ-Al_2O_3 catalyst. The first peak, around 430 °C, is generally attributed to the reduction of bulk NiO or NiO weakly interacting with the support. The broad high temperature reduction peak, at around 600 °C, can be ascribed to the reduction of NiO_x species that have stronger binding to the support. A third peak, at around 760 °C, is thought to be from the reduction of nickel aluminate based on literature precedence [27, 28]. In the case of alumina-supported nickel catalysts, it has been reported that nickel aluminate may form, which hinders complete reduction of the nickel species. Thus, in the present case, the third-peak can be associated with a nickel oxide layer that contacts the alumina surface [29, 30]. Reduction of the peak for the Ni/κ-Al_2O_3 catalyst at low temperatures was probably due to larger NiO particles and lower dispersion [14, 17]. The intensity and area of the first reduction peak shifted at lower temperatures in the following order: Ni/κ-Al_2O_3 < Ni/η-Al_2O_3 < Ni/γ-Al_2O_3 < Ni/θ-Al_2O_3 < Ni/δ-Al_2O_3. The nickel-support interaction depended on the type of support and nickel particle size. In addition, it was known that the size of nickel oxide particles affects its reducibility [31]. Generally, as the particle size of the active metal in the M/Al_2O_3 catalyst (M = active metal, such as Co, Ni, and Fe) increased, the intensity and area of the first reduction peak also tended to increase and shift to lower temperatures [32]. However, according to the XRD results presented in Table 2, the difference in NiO particle size for various Ni/Al_2O_3 catalysts was not significant. The TPR profiles showed that different alumina phases affected the reduction process. However, the reduction of NiO_x to Ni takes place at lower temperatures for Ni/γ-Al_2O_3, Ni/θ-Al_2O_3, and Ni/δ-Al_2O_3 catalysts compared with the Ni/η-Al_2O_3 catalyst.

H_2 chemisorption on Ni/Al_2O_3 catalysts provides valuable and quantitative information such as the number of nickel metal sites, nickel dispersion, and its average particle size. The results of H_2 chemisorption, including the metallic surface area, metal dispersion, and particle size, corrected using the reduction degree measured by O_2 titration, are presented in Table 2. The nickel particles, when corrected by considering the degree of reduction, were smallest (ca. 8.7 nm) in Ni/η-Al_2O_3. The particle size increased from 12.5 to 41.9 nm in the following order: Ni/η-Al_2O_3 < Ni/γ-Al_2O_3 < Ni/θ-Al_2O_3 < Ni/δ-Al_2O_3 < Ni/κ-Al_2O_3. Nickel particles sizes were in good agreement with the results of the XRD analysis, which showed the smallest Ni particles to be 8.7 nm, found in Ni/η-Al_2O_3, and the largest to be 41.9 nm, found in Ni/κ-Al_2O_3. By comparing the O_2 titrations of nickel oxide on different alumina phases for Ni/Al_2O_3 catalysts, the reduction degree was observed to be almost constant. The highly reduced nickel metal surface area could be correlated with enhancement of IPA conversion [4, 18]. Unreduced nickel oxides are not active in the reductive amination of IPA because they cannot catalyze the dehydrogenation-hydrogenation process [11]. The reduced metal surface area of nickel was largest for the Ni/η-Al_2O_3 catalyst at ca. 5.0 $m^2\ g^{-1}_{catalyst}$, which correlated with IPA conversion. Ni particle size in Ni/η-Al_2O_3 (8.7 nm) was shown to be smaller, therefore providing a higher surface area and

Table 2 Nickel particle size, surface area measured by H_2 chemisorption; reduction degree measured by O_2 titration

Catalysts	XRD		O_2 titration	H_2 chemisorption					H_2 TPR tempearature (°C)		
	Particle size of NiO (nm)	Particle size of Ni (nm)	Reduction degree (%)[a]	Uncorrected		Corrected		Metallic surface area (m^2 g_{cat}^{-1})	1 st peak (%)	2nd peak (%)	3rd peak (%)
				Dispersion (%)	Particle size (nm)	Dispersion (%)[b]	Particle size (nm)[c]				
Ni/θ-Al_2O_3	14.5	13.6	49.1	2.8	36.7	5.6	18.0	3.0	418 (44)	523 (47)	643 (9)
Ni/δ-Al_2O_3	14.2	15.0	48.4	2.4	42.9	4.9	20.8	2.7	420 (41)	525 (46)	660 (12)
Ni/η-Al_2O_3	9.6	8.7	48.5	4.4	23.0	9.1	11.2	5.0	369 (20)	544 (77)	746 (3)
Ni/γ-Al_2O_3	9.5	12.5	47.8	2.9	34.5	6.1	16.5	3.4	373 (13)	515 (75)	698 (12)
Ni/κ-Al_2O_3	18.0	18.7	48.4	1.2	86.6	2.4	41.9	1.3	368 (89)	480 (11)	

[a] Calculated from O_2 uptake

[b] Corrected dispersion (D) = Surface Ni^0 atom/total reduced Ni^0 atom × 100 = Surface Ni^0 atom/(total Ni atom × reduced fraction) × 100

[c] Corrected Ni diamete = Uncorrected Ni diameter × reduced Ni fraction

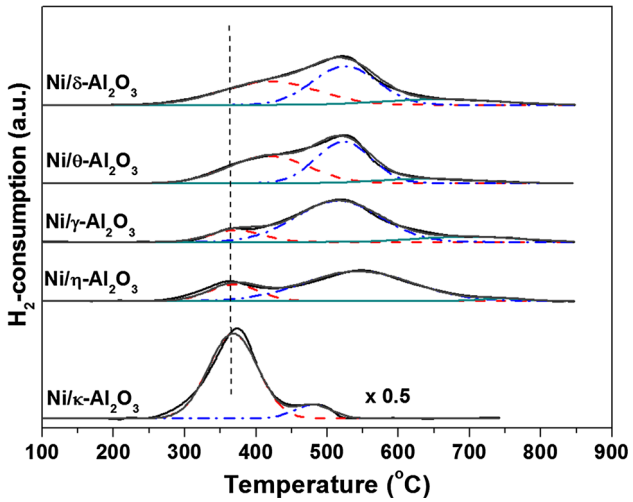

Fig. 4 H_2-TPR profiles of calcined Ni/Al_2O_3 catalysts with different alumina phase supports

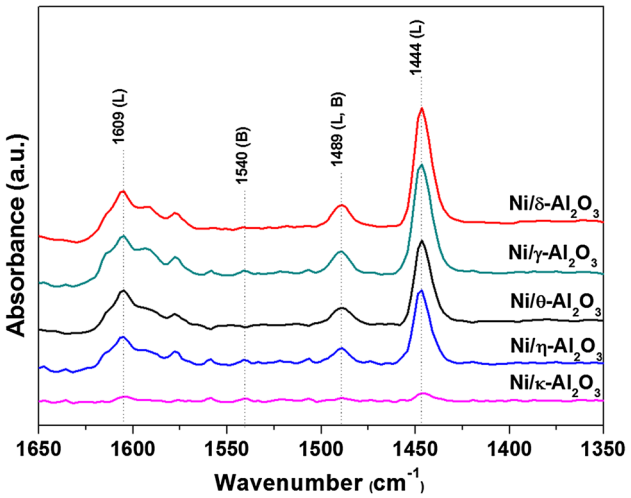

Fig. 5 FT-IR spectra of Ni/Al_2O_3 catalysts with different alumina phase supports after pyridine adsorption

larger Ni dispersion in comparison to other Ni/Al_2O_3 catalysts.

The FT-IR spectra recorded after pyridine adsorption at 50 °C were used to obtain information on the nature and amount of acid sites over various Ni/Al_2O_3 catalysts, as shown in Fig. 5. The bands from pyridine protonated by Brønsted acid sites appeared at 1540 cm^{-1}, while bands from pyridine coordinated to the Lewis acid sites, assigned to coordinatively unsaturated Al^{3+}, appeared at 1446 and 1605 cm^{-1}. The band at 1488 cm^{-1} indicates the formation of coupled Lewis and Brønsted acid sites. A band corresponding to α-pyridone species, representing the presence of basic surface OH groups and acid–base pair sites, also appeared at 1577 cm^{-1} [33–35]. The absence of bands around 1540 and 1640 cm^{-1} indicates that no Brønsted sites were present on the catalyst surface. The total amount of acid sites increased in the following order: $Ni/κ\text{-}Al_2O_3 < Ni/η\text{-}Al_2O_3 < Ni/θ\text{-}Al_2O_3 < Ni/δ\text{-}Al_2O_3 \approx Ni/γ\text{-}Al_2O_3$. We speculate that acidity had an important role in the product distribution over various Ni/Al_2O_3

catalysts, with high selectivity towards MIPA being associated with surface acidity.

Figure S1 shows the SEM images of Ni/Al_2O_3 catalysts. SEM was examined to observe the morphology and particle size of NiO over various Al_2O_3 supports. NiO particles of all catalysts showed a similar morphology as spherical shape. The average particle size is 8.6, 12.3, 18.3, 19.6 and 40.9 nm for Ni/η-Al_2O_3, Ni/γ-Al_2O_3, Ni/θ-Al_2O_3, Ni/δ-Al_2O_3, and Ni/κ-Al_2O_3 catalyst, respectively. The particle size increased from 8.6 to 40.9 nm in the following order: Ni/η-Al_2O_3 < Ni/γ-Al_2O_3 < Ni/θ-Al_2O_3 < Ni/δ-Al_2O_3 < Ni/κ-Al_2O_3. The dispersion of NiO is hardly observed by SEM images because it is difficult to classify between Ni and alumina. The energy dispersive X-ray Analysis (EDS) mapping of Ni/Al_2O_3 catalysts with various alumina supports was shown in Fig. S2. SEM/EDS mapping clearly reveals the higher dispersion of metallic Ni in Ni/η-Al_2O_3 and Ni/γ-Al_2O_3 more than Ni/κ-Al_2O_3. The dispersion was in good agreement with the results of the O_2 titration.

3.3 Reductive Amination of IPA

Table 3 shows the effect of the alumina phase on the reductive amination of IPA over Ni/Al_2O_3 catalysts. Results obtained with 30 min on stream were considered intrinsic activities. The catalysts showed no deactivation during this time. In our previous study, the deactivation of Ni/γ-Al_2O_3 catalyst was investigated in the presence or absence of hydrogen for the reductive amination of IPA [21]. The intrinsic catalytic activity for reductive amination of IPA under the reaction conditions studied here increased in the following order: Ni/δ-Al_2O_3 < Ni/κ-Al_2O_3 < Ni/θ-Al_2O_3 < Ni/γ-Al_2O_3 < Ni/η-Al_2O_3. Sewell et al. [36] and Chary et al. [13] suggested that alcohol conversion in reductive amination is proportional to the metal surface area, which is directly associated with metal dispersion. Although conversion was not directly proportional to the metallic surface area in the Ni/Al_2O_3 catalysts, the observed variation in conversion could be correlated with the differences in reduced metallic surface area in the catalysts. This was likely due to variations in reducibility and nickel metal dispersion that accompanied higher metallic surface areas [2], as shown by the H_2-chemisorption results (Table 2). The sums of the selectivities of MIPA, acetone, and DIPA were almost constant at ca. 100 % under the tested operating conditions. Acetone can be formed by dehydrogenation of IPA on metallic surface. Small quantities of DIPA were formed by a series reaction of MIPA with IPA by condensation/dehydration. An additional reversible reaction is DIPA + NH_3 → 2-MIPA [37]. DIPA can therefore be recycled in the reductive amination process. The MIPA selectivity of the Ni/Al_2O_3 catalysts was higher than acetone selectivity, except for Ni/κ-Al_2O_3. Among the catalysts, MIPA selectivity was lowest for the Ni/κ-Al_2O_3 catalyst. This was considered to be due to the overspread of large nickel particles on the outer surface of the κ-Al_2O_3 support. This meant that no acidic or basic sites were present on the κ-Al_2O_3 support. In the reductive amination mechanism for IPA, the first and last redox processes are catalyzed by the metal. In addition, the reaction of the acetone intermediate with NH_3 to form an imine does not require a metal catalyst, but can be accelerated over an acid or base catalyst [11, 38].

For the comparison study of MIPA selectivity over Ni/Al_2O_3 catalysts, the space velocity was maintained in the range 2.3–19.1 at 150 °C under identical reaction conditions. MIPA selectivity was dependent on the acidity of catalyst [6, 13], and the selectivity data was compared at constant IPA conversion (around 30 %) after 60 min of operation. The MIPA selectivities obtained are summarized in Table 4. The MIPA selectivity increased in the following order: Ni/κ-Al_2O_3 < Ni/η-Al_2O_3 < Ni/θ-Al_2O_3 < Ni/δ-Al_2O_3 ≈ Ni/γ-Al_2O_3. This result was in good agreement with the total number of acidic sites in the FT-IR spectra after pyridine adsorption (Fig. 6). IPA is dehydrogenated to acetone, subsequent conversion to carbinolamine by nucleophilic addition with ammonia, which in its turn is

Table 3 Effect of alumina phases in the reductive amination of IPA over Ni/Al_2O_3 catalysts

Catalysts	Conversion[a] (%)	Selectivity (%)[a]			MIPA yield (%)
		MIPA	Acetone	DIPA	
Ni/θ-Al_2O_3	35.9	73.1	20.3	6.6	26.2
Ni/δ-Al_2O_3	27.9	75.3	19.2	5.5	21.0
Ni/η-Al_2O_3	77.6	77.2	15.0	7.8	59.9
Ni/γ-Al_2O_3	62.1	78.2	15.0	6.8	48.6
Ni/κ-Al_2O_3	34.9	6.7	91.6	1.7	2.3

Reaction conditions: $T = 160$ °C, WHSV = 4.3 h^{-1}; feed compositions of IPA/NH_3/H_2/N_2 (mol. ratio) = 1/4/6/22.8

[a] Both conversion and selectivities to MIPA, acetone and DIPA obtained at 30 min on stream

Table 4 Product distributions at similar conversions of IPA over various Ni/Al_2O_3 catalysts

Catalysts	WHSV (h^{-1})	Conversion (%)	Selectivity (%)		
			MIPA	Acetone	DIPA
$Ni/\theta\text{-}Al_2O_3$	4.3	29.3	74.3	21.3	4.3
$Ni/\delta\text{-}Al_2O_3$	2.3	30.1	81.7	13.7	4.6
$Ni/\eta\text{-}Al_2O_3$	19.1	31.0	54.0	46.0	–
$Ni/\gamma\text{-}Al_2O_3$	11.1	32.6	82.0	16.9	1.1
$Ni/\kappa\text{-}Al_2O_3$	4.8	28.0	5.6	90.5	2.2

Reaction conditions: $T = 150$ °C, feed compositions of $IPA/NH_3/H_2/N_2$ (mol. ratio) = 1/4/6/22.8

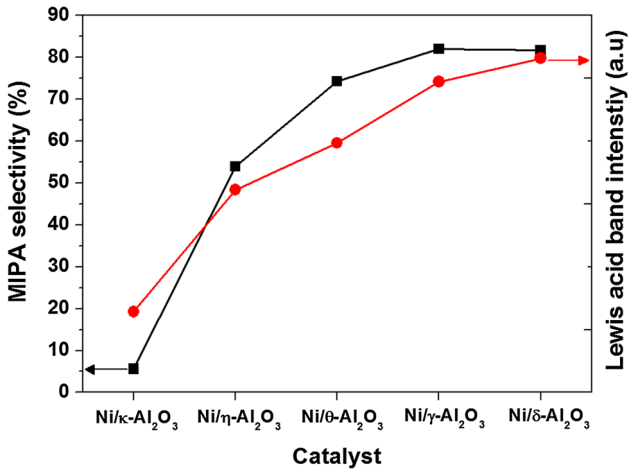

Fig. 6 Correlation between the Lewis acid band intensity and the MIPA selectivity for the reductive amination of IPA over Ni catalysts supported on various alumina phases

readily dehydrated to an imine [4]. Dehydration to the imine is considered a good measure of acidic or acid–base properties at the catalyst surface. We confirmed that no Brønsted sites were present on the catalyst surface by FT-IR spectra after pyridine adsorption. Kirumakki et al. [10] suggested that Brønsted acid (H^+) was found to be inactive in the reductive amination of alcohol. This means that the reaction proceeded at Lewis acid sites according to an E2 elimination mechanism. After adsorption of carbinolamine at the Lewis acid site, the base can attack it before dissociation, which could produce an iminium ion [39, 40]. It is important to evaluate the strength of Lewis acid sites based on the rate of dehydration to imine, which depends on the amount of formed imine for high selectivity toward MIPA. We speculated that high MIPA selectivity was due to the increase in the amount of adsorbed carbinolamine molecules, affected by the increase in the Lewis acid sites on the catalyst surface.

In our previous work, we examined the effect of nickel loading and reaction parameters (the effect of H_2, NH_3, reaction temperature, and space velocity) on the reductive amination of IPA over $Ni/\gamma\text{-}Al_2O_3$ catalysts and proposed optimal reaction conditions for $Ni/\gamma\text{-}Al_2O_3$ catalysts [21]. The long-term stability of $Ni/\eta\text{-}Al_2O_3$ and $Ni/\gamma\text{-}Al_2O_3$ catalysts was examined at 160 °C, with a space velocity of 2.3 h^{-1} and an R = [IPA]/[NH_3]/[H_2]/[N_2] molar ratio of 1:8:6:18.8, in the reductive amination of IPA over $Ni/\eta\text{-}Al_2O_3$ and $Ni/\gamma\text{-}Al_2O_3$ catalyst. The total flow rate was 50 cm^3 min^{-1}. The long-term stability of $Ni/\eta\text{-}Al_2O_3$ and $Ni/\gamma\text{-}Al_2O_3$ catalysts during the reductive amination of IPA is shown in Fig. 7. These catalysts, which showed the best catalytic activity and highest MIPA selectivity among the

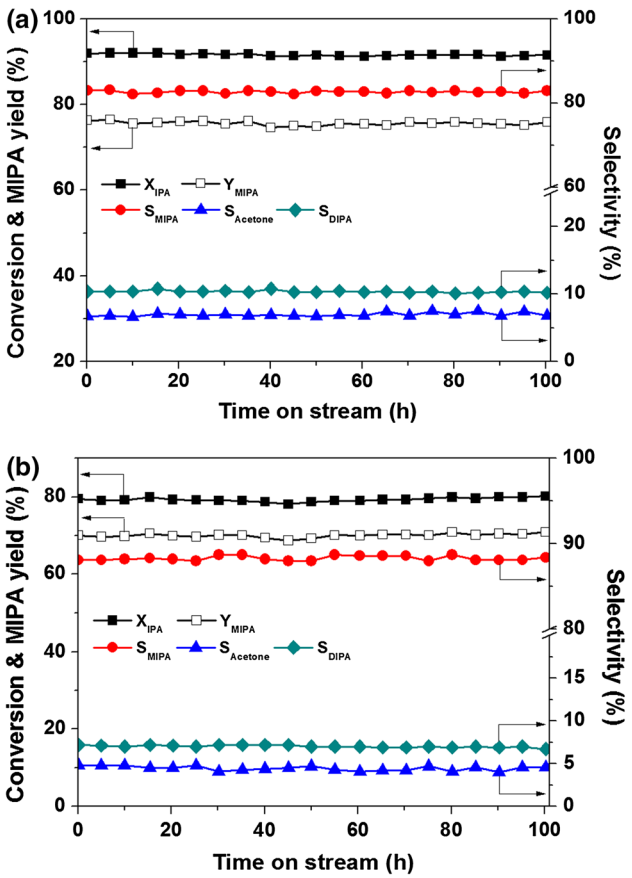

Fig. 7 Long-term stability of **a** $Ni/\eta\text{-}Al_2O_3$ and **b** $\gamma\text{-}Al_2O_3$ in the reductive amination of IPA. Reaction conditions: $T = 160$ °C, WHSV = 2.3 h^{-1}; feed composition of $IPA/NH_3/H_2/N_2$ (mol%) = 1/8/6/18.8

catalysts studied here, exhibited constant conversion to, and selectivity for, MIPA for up to 100 h on stream. These catalysts showed good catalytic activity and stability, and their excellent performance make the process economically viable.

4 Conclusion

Various alumina supports, such as θ-, δ-, η-, γ- and κ-Al_2O_3, influence the physicochemical and catalytic properties of nickel-based catalysts in the reductive amination of IPA. Ni/η-Al_2O_3 had the smallest nickel particle size and demonstrated the best catalytic performance, due to a high nickel metal surface area and high dispersion of nickel particles. The highest number of Lewis acid sites on the catalyst surface could be correlated with enhancement in the MIPA selectivity. The Ni/η- and γ-Al_2O_3 catalysts showed good catalytic performance in the reductive amination of IPA to MIPA.

Acknowledgments This work was supported by the Energy Efficiency and Resources of the Korea Institute of Energy Technology Evaluation and Planning (KETEP) granted financial resource from the Ministry of Trade, Industry and Energy, Republic of Korea (No. 2014021194).

References

1. Hayes KS (2001) Appl Catal A 221:187
2. Rausch AK, Steen E, Roessner F (2008) J Catal 253:111
3. Jeon HY, Shin C-H, Jung HJ, Hong SB (2006) Appl Catal A 305:70
4. Cho JH, Park JH, Chang TS, Seo G, Shin C-H (2012) Appl Catal A 417–418:313
5. Gardner DA, Clark RT (1981) US Patent 4,255,357
6. Huang Z-Y, Xu C-H, Liu C-Q, Xiao H-W, Chen J, Zhang Y-X, Lei Y-C (2013) Korean J Chem Eng 30:587
7. Seong M, Shin M, Cho J-H, Lee Y-C, Park Y-K, Jeon J-K (2014) Korean J Chem Eng 31:412
8. Majidian N, Habibi N, Rezaei M (2014) Korean J Chem Eng 31:1162
9. Dobson ID, Lidy WA, Williams PS (1990) US Patent 4,912,260
10. Kirumakki SR, Papadaki M, Chary KVR, Nagarajua N (2010) J Mol Catal A 321:15
11. Zamlynny V, Kubelkova L, Baburek E, Jiratova K, Novakova J (1998) Appl Catal A 169:119
12. Vedage GA, Emig LA, Li HX, Armor JN (1999) US Patent 5,917,092
13. Chary KVR, Seel KK, Naresh D, Ramakanth P (2008) Catal Commun 9:75
14. Rane S, Borg Ø, Yang J, Ryttera E, Holmen A (2010) Appl Catal A 388:160
15. Favaro L, Boumaza A, Roy P, Ledion J, Sattonnay G, Brubach JB, Huntz AM, Tetot R (2010) J Solid State Chem 183:901
16. Kim YH, Park ED (2010) Appl Catal B 96:41
17. Wang R, Li Y, Shi R, Yang M (2011) J Mol Catal A 344:122
18. Park JE, Park ED (2014) Korean J Chem Eng 31:1985
19. Shimizu K, Kenichi K, Onodera W, Yamazaki H, Kondo JN (2013) ACS Catal. 3:112
20. Park JE, Kim BB, Park ED (2015) Korea J Chem Eng 32:2212
21. Cho JH, Park JH, Chang TS, Kim J-E, Shin C-H (2013) Catal Lett 143:1319
22. Wang L, Li D, Koike M, Koso S, Nakagawa Y, Xu Y, Tomishige K (2011) Appl Catal A 392:248
23. Bae JW, Kim SM, Kang SH, Chary KVR, Lee YJ, Kim HJ, Jun KW (2009) J Mol Catal A 311:7
24. Kamal M, Khalil S (1998) J Catal 178:198
25. Elaloui E, Pierre AC, Pajonk GM (1997) J Catal 166:340
26. Oh JH, Bae JW, Park SJ, Khanna PK, Jun KW (2009) Catal Lett 130:403
27. Yang R, Li X, Wu J, Zhang X, Zhang Z, Cheng Y, Guo J (2009) Appl Catal A 368:105
28. Li C, Chen YW (1995) Thermochim Acta 256:457
29. Chen J, Ma Q, Rufford TE, Li Y, Zhu Z (2009) Appl Catal A 362:1
30. Ji Y, Zhao Z, Duan A, Jiang G, Liu J (2009) J Phys Chem C 113:7186
31. Prieto G, Martínez A, Concepción P, Tost RM (2009) J Catal 266:129
32. Park JY, Lee YJ, Khanna PK, Jun KW, Bae JW, Kim YH (2010) J Mol Catal A 323:84
33. Milewska JF, Decyk P, Ziolek M (2011) Appl Catal A 393:215
34. Kim YT, Jung KD, Park ED (2010) Microporous Mesoporous Mater 131:28
35. Kim YT, Jung KD, Park ED (2011) Appl Catal B 107:177
36. Sewell G, O'Connor C, Steen E (1995) Appl Catal A 125:99
37. Luyben WL (2009) Ind Eng Chem Res 48:10551
38. Fischer A, Maciejewski M, Burgi T, Mallat T, Baiker A (1999) J Catal 183:373
39. Turek W, Krowiak A (2012) Appl Catal A 417–418:102
40. Aramendia MA, Borau V, Jimenez C, Marinas JM, Porras A, Urbano FJ (1996) J Catal 161:829